JGR Planets

RESEARCH ARTICLE
10.1029/2022JE007672

Special Section:
The Mars Perseverance Rover Jezero Crater Floor Campaign

Dust Lifting Through Surface Albedo Changes at Jezero Crater, Mars

A. Vicente-Retortillo[1,2], G. M. Martínez[2,3], M. T. Lemmon[4], R. Hueso[5], J. R. Johnson[6], R. Sullivan[7], C. E. Newman[8], E. Sebastián[1], D. Toledo[9], V. Apéstigue[9], I. Arruego[9], A. Munguira[5], A. Sánchez-Lavega[5], N. Murdoch[10], M. Gillier[10], A. Stott[10], L. Mora-Sotomayor[1], T. Bertrand[11], L. K. Tamppari[12], M. de la Torre Juárez[12], and J.-A. Rodríguez-Manfredi[1]

[1]Centro de Astrobiología (INTA-CSIC), Madrid, Spain, [2]University of Michigan, Ann Arbor, MI, USA, [3]Lunar and Planetary Institute, USRA, Houston, TX, USA, [4]Space Science Institute, Boulder, CO, USA, [5]Física Aplicada, Escuela de Ingeniería, Universidad del País Vasco (UPV/EHU), Bilbao, Spain, [6]Johns Hopkins University Applied Physics Laboratory, Laurel, MD, USA, [7]CCAPS, Cornell University, Ithaca, NY, USA, [8]Aeolis Research, Chandler, AZ, USA, [9]Instituto Nacional de Técnica Aeroespacial (INTA), Madrid, Spain, [10]Institut Supérieur de l'Aéronautique et de l'Espace (ISAE-SUPAERO), Université de Toulouse, Toulouse, France, [11]LESIA, Paris Observatory, Meudon, France, [12]Jet Propulsion Laboratory, California Institute of Technology, Pasadena, CA, USA

Key Points:

- We identify surface albedo changes using Mars 2020 first-of-their-kind high-cadence in situ measurements of reflected solar radiation
- The most remarkable albedo changes observed within seconds outside dust storm conditions were caused by dust devils
- A multi-instrument analysis showed that the dust storm reduced surface albedo by more than 15%, primarily caused by dust removal

Supporting Information:

Supporting Information may be found in the online version of this article.

Correspondence to:

A. Vicente-Retortillo,
adevicente@cab.inta-csic.es

Citation:

Vicente-Retortillo, A., Martínez, G. M., Lemmon, M. T., Hueso, R., Johnson, J. R., Sullivan, R., et al. (2023). Dust lifting through surface albedo changes at Jezero Crater, Mars. *Journal of Geophysical Research: Planets*, *128*, e2022JE007672. https://doi.org/10.1029/2022JE007672

Received 14 NOV 2022
Accepted 12 MAR 2023

Abstract We identify temporal variations in surface albedo at Jezero crater using first-of-their-kind high-cadence in-situ measurements of reflected shortwave radiation during the first 350 sols of the Mars 2020 mission. Simultaneous Mars Environmental Dynamics Analyzer (MEDA) measurements of pressure, radiative fluxes, winds, and sky brightness indicate that these albedo changes are caused by dust devils under typical conditions and by a dust storm at $L_s \sim 155°$. The 17% decrease in albedo caused by the dust storm is one order of magnitude larger than the most apparent changes caused during quiescent periods by dust devils. Spectral reflectance measurements from Mastcam-Z images before and after the storm indicate that the decrease in albedo is mainly caused by dust removal. The occurrence of albedo changes is affected by the intensity and proximity of the convective vortex, and the availability and mobility of small particles at the surface. The probability of observing an albedo change increases with the magnitude of the pressure drop (ΔP): changes were detected in 3.5%, 43%, and 100% of the dust devils with $\Delta P < 2.5$ Pa, $\Delta P > 2.5$ Pa and $\Delta P > 4.5$ Pa, respectively. Albedo changes were associated with peak wind speeds above 15 $m \cdot s^{-1}$. We discuss dust removal estimates, the observed surface temperature changes coincident with albedo changes, and implications for solar-powered missions. These results show synergies between multiple instruments (MEDA, Mastcam-Z, Navcam, and the Supercam microphone) that improve our understanding of aeolian processes on Mars.

Plain Language Summary Small particles at the surface of Mars are lifted and transported through interactions with the atmosphere, modifying the fraction of solar radiation reflected by the surface (albedo). We analyzed the first albedo measurements acquired at 1 Hz and other environmental variables measured at Jezero crater, concluding that albedo changes are caused by dust devils under typical conditions and by a dust storm. The darkening of the surface induced by the storm is around 10 times larger than that caused in the absence of a storm by dust devils. Surface images indicate that this darkening is caused by dust removal. Only a fraction of the dust devils cause an albedo change, depending on their intensity, size and trajectory, and on the features of the small particles at the surface. The combined analysis of environmental variables, images and microphone recordings acquired by the Mars 2020 mission improve our understanding of the processes involved in the lifting and transport of small particles.

1. Introduction

The Martian atmosphere interacts with the surface, redistributing dust and sand particles (Kahre et al., 2017). Small particles are lifted by convective vortices and by strong wind gusts, and are subsequently transported before settling again (Basu et al., 2004; Kahre et al., 2006; Newman et al., 2002a, 2002b; Vicente-Retortillo et al., 2018). The redistribution of small particles modifies the surface albedo (Reiss et al., 2010; Szwast et al., 2006; Wells et al., 1984).

Since February 2021, the environmental conditions at Jezero crater (18.44°N, 77.45°E) have been monitored by the Mars Environmental Dynamics Analyzer (MEDA), the suite of meteorological sensors onboard the Mars 2020 Perseverance rover (Farley et al., 2020; Rodriguez-Manfredi et al., 2021). Simultaneous measurements from the Thermal and Infrared Sensor (TIRS), the Radiation and Dust Sensor (RDS), the Pressure Sensor and the Wind Sensor allow the study of dust lifting at the Martian surface by analyzing an unprecedented data set, including high frequency measurements (1–2 Hz) of surface broadband albedo and temperature, wind speed and direction, downwelling radiation, sky radiance, and pressure. In addition, Mastcam-Z (Bell et al., 2021) and Navcam (Maki et al., 2020) images allow quantitative estimations of the spectral reflectance of the surface and provide additional visual context of the rover surroundings. Finally, recordings of the Supercam microphone (Maurice et al., 2021) provide additional information on winds during some periods for which MEDA winds are not available.

Surface albedo changes have typically been analyzed using satellite measurements (Cantor et al., 2006; Fenton et al., 2016; Geissler et al., 2016; Reiss et al., 2016; Szwast et al., 2006; Wellington & Bell, 2020; Whelley & Greeley, 2008). These studies provide relevant information about the temporal and spatial variability of dust lifting processes. However, satellite observations generally lack contemporaneous near-surface environmental measurements and have a low temporal coverage at a given location. Albedo has also been studied using images acquired by landed missions (Baker et al., 2021; Bell et al., 2008; Charalambous et al., 2021; Greeley et al., 2005; Rice et al., 2018). Such images provide a good contextual view of the terrain but would require vast amounts of power and data storage if taken every second. Hence, albedo studies from imaging typically focus on spatial variations (rovers) or temporal variations within various sols (landers).

The combination for the first time of high-frequency and simultaneous albedo and environmental MEDA measurements allows for unambiguous attribution of the atmospheric events inducing the albedo changes; in addition, environmental variables coincide temporally and spatially with these events, providing the pressure and wind conditions during the albedo change, which are useful for setting thresholds in numerical models; moreover, our multi-instrument approach includes an analysis of temporal variations in surface spectral reflectance from Mastcam-Z images, allowing to assess whether the albedo change is caused by dust removal or by redistribution of coarser grain sand.

Jezero crater was affected by a large regional dust storm between sols 313 and 318 of the mission ($L_s \sim 155°$; 5–10 January 2022; Malin & Cantor, 2022), which caused a significant change in environmental conditions. The rover remained at the same location between sols 287 and 328, providing a unique opportunity to study the surface albedo and temperature before, during, and after the storm.

Section 2 describes the Mars 2020 instruments that provided the measurements for this work and the methodology to analyze the albedo changes. Sections 3 and 4 are devoted to the surface albedo changes under typical conditions and during a dust storm, respectively. In Section 5, we provide an overall discussion covering dust lifting thresholds, dust removal estimations, simultaneous surface temperature variations and implications for solar-powered missions. Section 6 summarizes the main results.

2. Materials and Methods

2.1. Mars 2020 Instruments Used in This Work

We used four MEDA sensors in this study, as described above. TIRS (Sebastián et al., 2020, 2021) comprises five channels which measure downward (IR1) and upward (IR4) longwave (6.5–30 μm) radiative fluxes, atmosphere temperature (IR2), reflected shortwave (0.3–3 μm) radiation (IR3), and surface temperature (IR5). Channels IR3, IR4, and IR5 cover a surface area of about 3 m^2 located less than 4 m from the RTG to avoid thermal contamination (Pérez-Izquierdo et al., 2018; Rodríguez-Manfredi et al., 2021). These channels have a field of view (FOV) of ±20° in the horizontal and ±10° in the vertical, with a pointing elevation of ±35°. Figure S1 illustrates the TIRS FOV. The RDS has two sets of eight photodiodes. The TOP photodiodes point toward the zenith and include a detector (TOP7) with a hemispheric FOV that measures downwelling shortwave radiation between 190 and 1,100 nm (Apéstigue et al., 2022; Rodríguez-Manfredi et al., 2021). The second set of photodiodes (LAT) point at an elevation of 20° (or 35° for LAT8), pointing at azimuth angles separated 45° (note that LAT1 is blind and is used to characterize the degradation due to the radiation environment); approximately, LAT1, LAT 3, LAT5, and LAT7 point toward the front, left, rear and right of the rover, respectively; the pointing directions of the lateral channels are illustrated in Apéstigue et al. (2022), Newman et al. (2022), and Toledo et al. (2023). The

wind sensor consists of two booms at about 1.5 m above the ground, separated by 120° in azimuth to mitigate the effects of hardware interfering with the flow (Rodríguez-Manfredi et al., 2021). These variables are complemented by measurements with the pressure sensor (Harri et al., 2014).

MEDA albedo measurements were complemented by images acquired by the Mastcam-Z and Navcam cameras. Mastcam-Z is a stereo imaging system that uses a pair of CCD cameras with superimposed red, green, and blue filtered microlenses arranged in a Bayer pattern (Bell et al., 2021). The two Navcams (navigation cameras) acquire color stereo images of the surface with a 96° × 73° FOV (Maki et al., 2020). The Supercam microphone records air pressure fluctuations with a sampling rate up to 100,000 Hz at a height of ∼2.1 m above the Martian surface (Maurice et al., 2021). The microphone can be considered as a high frequency wind speed sensor because the intensity of the microphone signal in the 20 Hz to 1 kHz bandwidth is strongly correlated with the wind speed (Chide et al., 2021; Maurice et al., 2021).

2.2. Detection of Albedo Changes and Dust Devil Encounters

We use the ratio between TIRS IR3 and RDS TOP7 measurements as a proxy for surface albedo (note that the values do not correspond to the actual albedo because TIRS and RDS measure in different spectral bands, but it is valid for our purpose of analyzing relative temporal variations; actual albedo values accounting for the difference in bands are shown in Martínez et al., 2023). We have applied two different methods to detect albedo changes. The first relies on sol-to-sol comparisons of albedo values at different local times centered at noon. The main advantage of this method is that it allows the detection of albedo changes even if the albedo change took place while the albedo was not being measured (during nighttime or when MEDA is powered off).

When the rover drives are frequent, sol-to-sol comparisons at a given location are scarce, not allowing the detection of surface albedo temporal changes. MEDA measurements show the passage of numerous convective vortices close to the rover, which are detected as pressure drops (Hueso et al., 2023; Newman et al., 2022). Some of these drops are accompanied by a decrease in downward shortwave radiation and changes in sky brightness, indicating that the convective vortex contains significant dust, which must have been lifted previously from the surface, and is therefore a dust devil. The second method to detect albedo changes relies on the analysis of simultaneous measurements of pressure, radiation, sky brightness, and wind to identify the dust devils that are more likely to have affected the closest surroundings of the rover and compare the albedo in the surface portion covered by TIRS before and after the passage of each of these dust devils.

In order to estimate the albedo change with this second method, we perform the following steps. First, we select the measurement session corresponding to each of these dust devils. Then, we calculate two 2nd-degree polynomial fits, one for the measurements at the beginning of the session and 1 minute before the pressure drop induced by the dust devil, and another one for the measurements between 1 minute after the pressure drop and the end of the session. The selection of a 2nd-degree polynomial allows a good fit to the albedo observations, which show a marked parabolical diurnal evolution (Martínez et al., 2023). Then, we assess the occurrence of an albedo change by calculating two values: The difference between the measurements acquired between 1 and 5 min before and after the pressure drop and the polynomial fits obtained from the measurements after and before the pressure drop, respectively. Then, we visually inspect the measurements and the fits and determine the most reliable value (when the number of measurements between the pressure drop and any of the extremes of the session is small, the polynomial obtained with those measurements may not fit well the remaining of the session; this also applies when there is rover motion during the session). If both values are reliable, we follow a conservative approach and select the one showing a smaller albedo change. Since we are analyzing relative variations within minutes, the uncertainty of the albedo change is estimated from the standard deviation of the differences between the measurements and the fits, which is 0.10%–0.15%. In some cases when the dust devil passage occurred close to the extremes of the session or to rover motion or under conditions of high variability in radiation measurements, the assessment of the albedo change was not conclusive (N.C.).

Finally, we list the unambiguous albedo changes, defined as those exceeding 0.5%. This threshold has been selected to maximize the confidence in the detected changes, since it is above three times larger than the estimated uncertainty in the albedo change, and therefore the distributions of the individual (1 Hz) measurements before and after the albedo change are unambiguously distinguishable; a lower threshold could lead to the inclusion of false positives, and a higher threshold could lead to the lack of identification of subtle actual albedo changes.

2.3. Analysis of Surface Albedo From Mastcam-Z Observations

MEDA measurements are extremely useful for the study of the environmental conditions that can cause a surface albedo change. However, they do not provide information on whether the albedo change was caused by dust removal or by redistribution of coarser sands. In order to address this question, we use Mastcam-Z observations. These observations allow the identification of albedo changes by comparing images of the same target acquired under very similar conditions. In addition, they provide information on the spectral reflectance using the blue, green and red Bayer filters, characterized by effective wavelengths of 480, 544, and 630 nm (respectively) and half-width at half-maximum values between 41 and 46 nm (Bell et al., 2021; Merusi et al., 2022). From these three reflectance values it is possible to calculate the green Bayer filter band depth in a way analogous to Jacob et al. (2020):

$$\mathrm{BD}_g = 1 - \left(R^*_{544} / \left(0.573 \cdot R^*_{480} + 0.427 \cdot R^*_{630}\right)\right) \quad (1)$$

R^* is the relative reflectance, which is the radiance factor (the ratio between the scene radiance and the total solar irradiance) divided by the solar incidence angle (Reid et al., 1999; Rice et al., 2022). This spectral parameter is related to a ferric iron absorption band which is typically present in dusty surfaces (e.g., Farrand et al., 2006; Johnson, Grundy, et al., 2006; Morris et al., 2000; Rice et al., 2022). Hence, temporal changes in dust cover at the surface can be monitored using a combination of variations in the green Bayer filter band depth images and overall visible changes in surface spectral and spatial properties.

3. Surface Albedo Changes in the Absence of Dust Storms

In this section, we study the surface albedo changes detected during the first 350 sols of the Mars 2020 mission, excluding sols 313 to 318, when the rover was affected by a dust storm (Section 4). During the period outside the dust storm, sol-to-sol comparisons of albedo values have allowed the detection of several unambiguous surface albedo changes. Most of the changes in the TIRS IR3 to RDS TOP7 ratio were caused by a change in the rover position or by the motion of the robotic arm or the remote sensing mast. However, some of these changes were not explained by these factors, indicating actual albedo changes in the region observed by TIRS.

Analysis of albedo measurements revealed that surface changes occurred suddenly (within a few seconds) and were persistent. Figure 1 shows an example of an albedo change on sol 57 (other albedo changes are listed in Table 1). The top left panel shows the albedo measurements on sol 57 (red); the comparison with nearby sols (55 and 59) shows an unambiguous decrease in albedo. The panel on the right shows the environmental variables for the 2 minutes surrounding the pressure minimum of the dust devil that caused the change in albedo: the dust devil, characterized by a pressure drop above 2.5 Pa (a), induced a reduction in surface brightness attributed to dust removal that is indicated by the relative differences between the downward (blue) and reflected (green) shortwave fluxes (b) after the dust devil encounter; the pressure drop is coincident with simultaneous changes in sky brightness detected by various lateral channels (c), which primarily indicate increased scattering from a briefly dusty region of atmosphere, and with a peak in wind speed (d), indicating that the dust devil surrounded the rover; (e) shows the decrease in surface temperature and the increase in downwelling longwave radiation, attributed to the lofting of small particles by the convective vortex. The bottom left panel corresponds to a Navcam image showing the TIRS FOV at that location.

We note that all of a sudden and persistent albedo changes showed similar simultaneous pressure drops, indicating that they were caused by dust devils. This suggests that albedo changes caused by wind gusts are less frequent during the period covering the first 350 sols of the mission outside the dust storm. Although none of the unambiguous albedo changes in the surface observed by TIRS occurred in the absence of a dust devil, a distant gust lifting event was observed at Jezero on sol 117 (Newman et al., 2022).

We have detected more than 80 dust devils (some of them corresponding to the dust storm period) for which environmental variables suggest that they surrounded the rover or at least passed at a distance small enough to be detected simultaneously in pressure and various LAT channels (like in Figures 1a and 1c). We analyzed the surface albedo around these events, concluding that 12 of them showed unambiguous (>0.5%) albedo changes. Table 1 summarizes the features of the selected dust devils that could induce changes in surface albedo based on their proximity to the rover; terrain properties are also included (Martínez et al., 2023). The change of each variable is calculated as the maximum difference within 30 s of the pressure minimum between observations and a fit obtained using a moving median with a temporal window of 2 minutes. The magnitude of the changes and of the processed maximum wind speeds could be interpreted as a lower bound. In the case of wind speed, processed data (archived in the NASA Planetary Data System as DER_WS files) at any moment are obtained from the

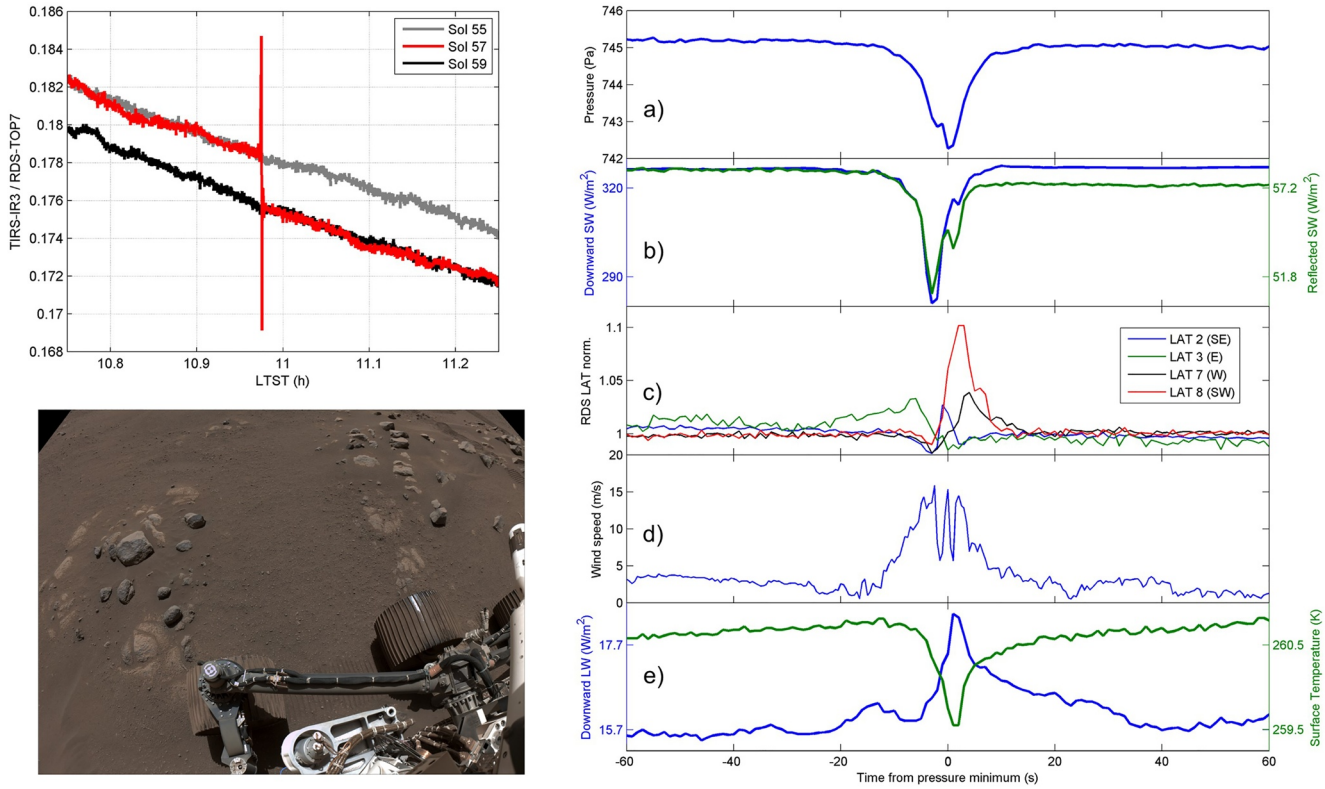

Figure 1. (top left) Surface albedo between 10:45 and 11:15 LTST on sols 55 (gray), 57 (red), and 59 (black) of the Mars 2020 mission. There is a sudden albedo change on sol 57, which is caused by a dust devil. (Bottom left) Navcam image showing the Thermal and Infrared Sensor (TIRS) field of view (FOV) and its surroundings at the rover's location between sols 52 and 65 (see Figure S1 for additional details on the TIRS FOV at selected locations). Details in Table 2. (right) Environmental variables measured by Mars Environmental Dynamics Analyzer during the passage of the dust devil that caused the albedo change: (a) pressure; (b) shortwave downward (blue) and reflected (green) radiation; (c) normalized measurements of the RDS lateral channels 2, 3, 7, and 8; the rover was heading toward the South, implying that the channels are approximately pointing toward the Southeast, East, West and Southwest, respectively; (d) wind speed; (e) downward longwave radiation (blue) and surface temperature (green). The reader is referred to the text for the interpretation of these panels.

boom that most closely points into the incoming winds (the one less affected by the rover) and after the removal of wind speed variations above 5 m/s within one second (Newman et al., 2022). The selection of 5 m/s can be justified by analyzing the measured wind speed changes within 1 s from both booms (measurements from both booms are archived as CAL_WS files), obtaining a three-sigma value of 4 m/s from a distribution of around 10 million measurements. The removal of these strong variations in wind speed causes some gaps in the data set; we have represented the wind measurements for each dust devil, and we have specified the cases for which gaps are contiguous to the maximum wind speed. Wind speed measurements are included until the dust storm, when sand grain impacts during this period of increased aeolian activity damaged the MEDA wind sensor.

As shown in Table 1, the albedo changes induced by dust devils are between 0.5% and 2.1%. All of the unambiguous changes correspond to a decrease in albedo; the implications of this behavior are further discussed in Sections 4 and 5. A common feature of the dust devils that caused an albedo change is their intensity, indicated by pressure drops and wind speeds above average. The majority of the dust devils causing albedo changes showed pressure drops greater than 2.5 Pa (indicating that these were strong events; Newman et al., 2022) and peak wind speeds above 15 m/s. In addition, most of these dust devils lifted large amounts of dust, leading to decreases in downwelling solar radiation of typically around 10% but up to 25%. However, there are various dust devils with similar features that have not caused a clear change in albedo. This will be discussed further in Section 5.

4. Surface Albedo Changes During the Dust Storm

During the first week of 2022, a large regional dust storm moved north from southern mid-latitudes, crossed the equator and affected the Jezero crater (Malin & Cantor, 2022). During this storm, dust opacities at 880 nm

Table 1
Features of the Selected Dust Devils That Could Induce Changes in Surface Albedo Based on Their Proximity to the Rover

Sol	LTST	ΔAlbedo (%)	ΔP (Pa)	ΔDSW (%)	ΔT (K)	WS (m/s)	Albedo at noon	TI (tiu)
32	13.85	<|−0.5|	−0.7	−0.1	−0.6	–	–	–
34	12.5	<|−0.5|	−2.0	−0.9	<|−0.2|	–	–	–
37	14.23	<|−0.5|	−1.2	−1.0	−0.3	>18.3	0.12	310
37	14.47	<|−0.5|	−0.6	−0.2	<|−0.2|	14.2	0.12	310
45	11.56	<|−0.5|	−0.4	−1.0	<|−0.2|	–	0.12	310
45	12.98	<|−0.5|	−0.4	−4.9	−0.3	>15.8	0.12	310
48	13.74	<|−0.5|	−0.4	−0.6	<|−0.2|	8.6	–	–
57	**10.98**	**−1.5**	**−2.8**	**−13.9**	**−1.1**	**15.9**	**0.12**	**350**
57	12.65	<|−0.5|	−3.4	−13.1	−0.3	>18.0	0.12	350
61	12.66	<|−0.5|	−1.5	−0.4	<|−0.2|	11.8	0.12	350
71	12.96	<|−0.5|	−0.7	−1.3	<|−0.2|	13.6	–	–
81	12.94	<|−0.5|	−1.3	−2.2	<|−0.2|	11.0	0.12	315
82	**12.08**	**−2.1**	**−5.6**	**−12.7**	**−1.8**	**19.0**	**0.12**	**320**
84	10.78	<|−0.5|	−3.4	−2.4	−0.7	18.4	–	–
85	15.58	<|−0.5|	−2.2	−1.2	<|−0.2|	15.3	0.12	365
89	14.97	N.C.	−2.8	−2.9	−0.3	–	0.13	700
99	15.27	<|−0.5|	−2.3	−1.7	<|−0.2|	–	–	–
106	13.01	N.C.	−2.1	−2.8	−0.3	18.9	0.13	180
106	13.03	N.C.	−0.6	−2.7	<|−0.2|	9.8	0.13	180
110	14.54	<|−0.5|	−3.1	−1.6	<|−0.2|	>13.4	–	–
111	13.63	<|−0.5|	−0.6	−0.7	<|−0.2|	15.9	0.13	290
112	**12.45**	**−0.7**	**−1.4**	**−1.5**	**−0.6**	**17.2**	**0.13**	**290**
113	13.97	N.C.	−1.1	−0.9	<|−0.2|	13.6	–	–
114	11.05	<|−0.5|	−0.4	−2.3	<|−0.2|	11.2	0.12	265
117	12.73	<|−0.5|	−0.4	−0.4	<|−0.2|	16.0	0.14	325
119	11.71	<|−0.5|	−3.6	−3.1	−0.6	16.0	0.14	330
125	13.11	<|−0.5|	−1.5	−0.7	<|−0.2|	-	0.16	605
128	**12.36**	**−0.5**	**−3.5**	**−7.2**	**−0.5**	**22.4**	–	–
160	10.99	<|−0.5|	−1.0	−0.4	<|−0.2|	9.1	0.12	380
161	**13.96**	**−0.8**	**−3.9**	**−6.5**	**−0.3**	**>16.8**	**0.12**	**365**
166	**13.09**	**−0.6**	**−5.0**	**−12.9**	**−1.2**	**22.4**	–	–
169	11.79	<|−0.5|	−0.4	−1.4	−0.3	13.1	–	–
173	**15.64**	**−0.6**	**−0.6**	**−1.6**	**−0.5**	**21.0**	–	–
174	10.92	<|−0.5|	−2.2	−2.8	−0.3	>15.8	0.12	275
177	11.64	<|−0.5|	−2.0	−4.1	<|−0.2|	10.9	–	–
179	10.85	<|−0.5|	−0.4	−2.7	<|−0.2|	13.9	–	–
184	12.88	<|−0.5|	−2.1	−4.0	−0.7	18.3	–	–
187	12.12	<|−0.5|	−0.6	−1.2	<|−0.2|	12.2	0.12	230
188	13.1	<|−0.5|	−2.8	−4.6	−0.8	20.8	0.12	230
197	15.45	<|−0.5|	−1.1	−0.8	<|−0.2|	16.6	0.12	225
198	11	<|−0.5|	−1.5	−1.6	−0.3	>17.0	0.12	230
208	12.6	<|−0.5|	−4.3	−1.4	−0.5	>18.3	–	–
211	12	<|−0.5|	−2.6	−3.3	−0.6	>16.1	0.14	425

Table 1
Continued

Sol	LTST	ΔAlbedo (%)	ΔP (Pa)	ΔDSW (%)	ΔT (K)	WS (m/s)	Albedo at noon	TI (tiu)
213	12.24	N.C.	−2.3	−21.0	−0.8	24.6	–	–
213	12.34	<|−0.5|	−0.8	−0.6	−0.4	>23.6	–	–
215	10.31	<|−0.5|	−0.3	−4.9	−0.2	12.2	0.14	410
215	11.04	<|−0.5|	−1.9	−0.7	<|−0.2|	10.7	0.14	410
237	11.61	<|−0.5|	−1.7	−8.5	<|−0.2|	>8.2	0.14	425
242	**13.49**	**−0.5**	**−2.6**	**−1.3**	**−0.2**	**17.8**	**0.12**	**700**
265	11.95	<|−0.5|	−0.5	−2.8	<|−0.2|	14.7	0.13	375
265	12.01	<|−0.5|	−1.0	−0.9	<|−0.2|	18.5	0.13	375
266	11.18	<|−0.5|	−0.4	−0.5	<|−0.2|	15.77	0.14	370
271	11.76	<|−0.5|	−0.5	−1.7	<|−0.2|	9.3	0.13	375
280	11.42	<|−0.5|	−1.9	−0.6	<|−0.2|	13.5	–	–
280	13.5	<|−0.5|	−3.0	−5.8	−0.5	15.7	–	–
284	**10.62**	**−0.8**	**−4.8**	**−10.0**	**−3.0**	**>14.5**	–	–
284	13.19	<|−0.5|	−1.9	−12.1	−1.4	>15.0	–	–
305	13.64	<|−0.5|	−4.3	−6.9	−1.2	>12.7	0.11	295
306	11.12	<|−0.5|	−3.8	-	−0.9	>18.5	0.11	300
309	14.42	<|−0.5|	−2.9	−0.9	<|−0.2|	14.7	0.11	290
310	14.94	<|−0.5|	−1.1	−0.5	<|−0.2|	10.3	0.11	305
311	**12.29**	**−1.3**	**−4.6**	**−24.9**	**−1.8**	**>14.3**	**0.11**	**290**
313	10.38	<|−0.5|	−0.4	−2.4	−0.9	24.7	0.11	310
314	10.99	N.C.	−2.1	−7.5	−0.9	–	0.11	320
315	10.01	<|−0.5|	−1.0	−2.7	−0.4	–	0.11	315
315	10.58	<|−0.5|	−1.5	−4.7	−0.3	–	0.11	315
315	12.41	<|−0.5|	−0.9	−1.9	<|−0.2|	–	0.11	315
316	13.57	<|−0.5|	−0.4	−3.2	<|−0.2|	–	0.10	330
316	14.63	<|−0.5|	−0.6	−2.5	<|−0.2|	–	0.10	330
320	13.49	<|−0.5|	−0.4	−0.4	−0.2	–	0.09	315
320	13.97	<|−0.5|	−0.7	−0.5	<|−0.2|	–	0.09	315
321	15.02	<|−0.5|	−2.4	−1.1	<|−0.2|	–	0.09	315
321	15.14	<|−0.5|	−2.3	−2.3	−0.4	–	0.09	315
323	11.93	<|−0.5|	−1.5	−2.0	−0.4	–	0.09	315
323	15.83	<|−0.5|	−2.2	−0.9	<|−0.2|	–	0.09	315
324	15.22	<|−0.5|	−1.9	−2.8	<|−0.2|	–	0.09	325
325	13.4	<|−0.5|	−1.3	−3.8	<|−0.2|	–	0.09	320
325	13.48	<|−0.5|	−1.6	−0.6	−0.2	–	0.09	320
327	**13.03**	**−1.3**	**−6.1**	**−20.8**	**−1.3**	–	**0.09**	**315**
333	12.34	<|−0.5|	−0.4	−1.7	<|−0.2|	–	–	–
337	15.9	<|−0.5|	−1.0	−1.6	<|−0.2|	–	0.12	365
344	10.82	<|−0.5|	−3.1	−1.6	−0.3	–	0.10	350
346	10.94	<|−0.5|	−1.0	−1.1	−0.4	–	0.10	350

Table 1
Continued

Sol	LTST	ΔAlbedo (%)	ΔP (Pa)	ΔDSW (%)	ΔT (K)	WS (m/s)	Albedo at noon	TI (tiu)
349	**12.17**	**−1.1**	**−2.5**	**−7.3**	**−0.6**	–	**0.10**	**350**
350	10.88	<|−0.5|	−3.9	−4.4	−0.4	–	–	–

Note. Columns indicate sol number, local time, magnitude of the albedo change (N.C. indicates that the analysis is inconclusive), transient drops in pressure (P), downwelling shortwave radiation (DSW) and surface temperature (T), peak wind speed, albedo at noon and thermal inertia. Bold highlights dust devils with surface albedo changes.

measured by Mastcam-Z around noon increased from less than 0.4 on sol 312 to almost 1.4 on sol 316, decreasing again to 0.4 on sol 319 (Figure 2a). Perseverance remained at the same location between sols 287 and 328, providing a unique opportunity to track surface albedo before, during, and after the storm.

Figure 2a shows the temporal evolution of the surface albedo between sols 287 and 328 at 13 LMSTs (a similar behavior is observed at other local times). The most remarkable feature shown in this panel is the strong darkening of the surface induced by the dust storm: there was a 17% decrease in surface albedo between sols 315 and 319; the largest sol-to-sol variation occurred between sols 315 and 316, when the albedo decreased to 11%. In contrast, the albedo remained stable both before and after the storm. Figures 2b and 2c provide additional context showing the surface FOV observed by TIRS. In particular, evidence of aeolian processes was manifested by the subdued appearance of the wheel tracks after the storm. This will be further discussed below.

In order to quantitatively assess the changes induced by the dust storm, we used Mastcam-Z pairs of images of portions of the surface observed by TIRS (Figure 3). Both images of each pair were acquired under similar times of sol (Table 2), radiometrically calibrated to relative reflectance (cf. Bell et al., 2021; Hayes et al., 2021), and paired images were stretched identically (Table 2). This enables differences in each pair of images to be interpreted as changes in albedo, which could be attributed to removal of dust (reddish, fine-grained airfall materials) or by transport of coarser-grained sands.

In Figures 3a and 3b, the rover wheel tracks appeared morphologically fainter following the dust storm, suggesting that small particles making up the molded tracks were mobilized. However, there is also an overall relative darkening and loss of reddish appearance in the images acquired after the storm. This is supported by the quantitative analysis shown in Figure 3e, where the relative reflectance of the wheel track (red box in Figure 3a)

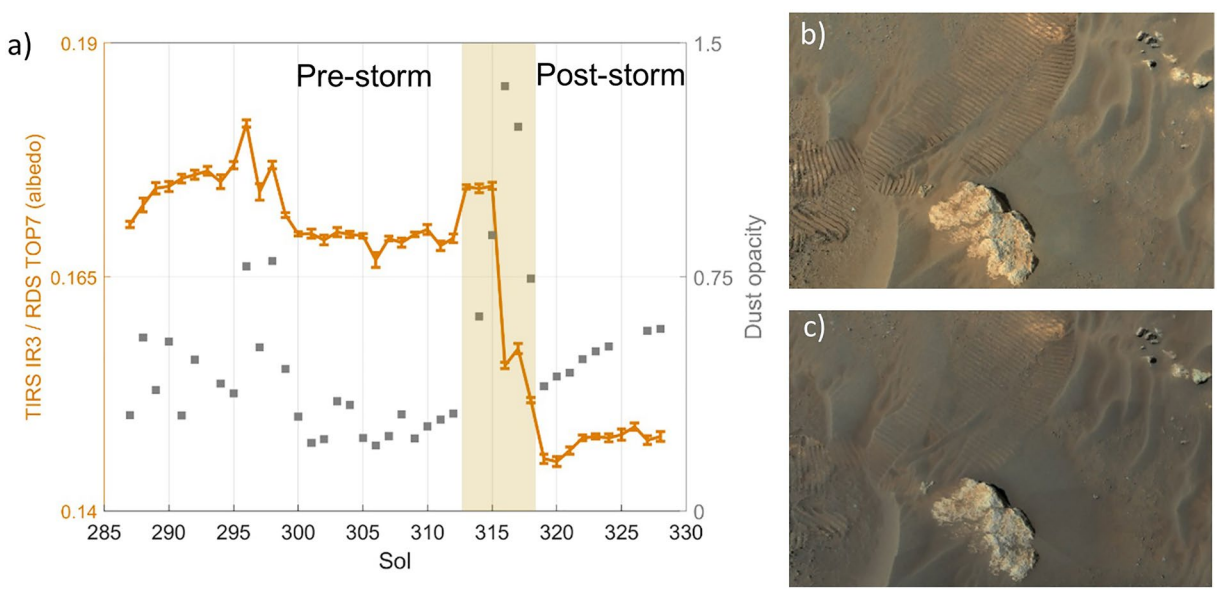

Figure 2. (a) Change in surface albedo at 13:00 LMST (dark orange) and dust opacity around noon (gray) between sols 287 and 328. (b, c) Comparison of portions of Mastcam-Z vertical projection mosaics corresponding to the Thermal and Infrared Sensor field of view before (b) and after (c) the dust storm.

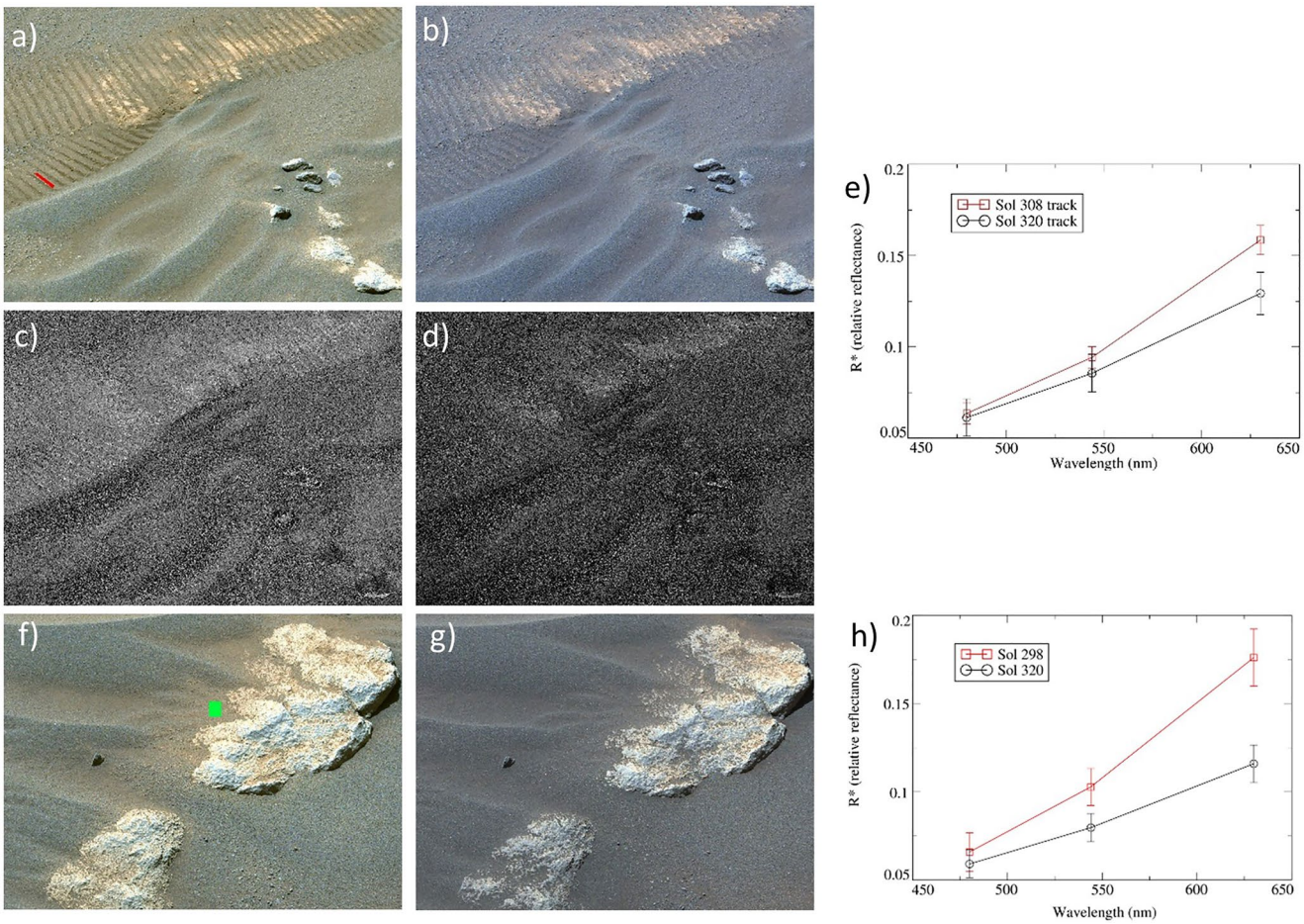

Figure 3. (a, b) Mastcam-Z Bayer filter image of the wheel tracks in the Thermal and Infrared Sensor (TIRS) field of view (FOV) before (a) and after (b) the storm; (c, d) Green Bayer filter band depth images corresponding to (a, b) images, respectively; (e) Comparison of Bayer-filter (3-band) relative reflectance spectra of rover track (red box in (a)) from before and after the storm; (f, g) Mastcam-Z bayer filter image of region within the TIRS FOV before (f) and after (g) the storm; (h) Comparison of Bayer-filter relative reflectance spectra of regolith (green box in (f)) from before and after dust storm. Details on images are provided in Table 2.

Table 2
Summary of the Acquisition Time, Image ID and Processing Details of the Images Shown in Figures 1–3

Fig.	Acq. time	Image ID	Processing details
1,b.l.	Sol 64 13:54 LMST	NLF_0064_0672627159_178CWS_N0032046NCAM00201_0A0195J01	
2b	Multiple sols 286-312		Portion of Mastcam-Z vertical projection mosaics
2c	Multiple sol 320		As in 2b
3a	Sol 308 11:53 LMST	ZL0_0308_0694280717_269IOF_N0090000ZCAM08334_0340LMA03	Calibrated to relative reflectance and stretched red = 0.00–0.27; green = 0.00–0.17; blue = 0.00–0.11
3b	Sol 320 12:20 LMST	ZL0_0320_0695347646_895IOF_N0090000ZCAM08341_0340LMA01	As in 3a
3c	As in 3a	As in 3a	Stretched 0.00–0.20
3d	As in 3b	As in 3b	As in 3c
3f	Sol 298 12:54 LMST	ZL0_0298_0693396692_898IOF_N0090000ZCAM08323_0340LMA02	Calibrated to relative reflectance and stretched red = 0.00–0.32; green = 0.00–0.20; blue = 0.00–0.14
3g	Sol 320 12:19 LMST	ZL0_0320_0695347593_895IOF_N0090000ZCAM08341_0340LMA01	As in 3f

decreased in the three Bayer wavelengths after the storm. From these three reflectance values, a green Bayer filter band depth was calculated as described in Section 2. The Bayer images in Figures 3a and 3b were stretched identically, as were their corresponding green filter band depth maps in Figures 3c and 3d (Table 2). The post-storm Bayer images are darker and less red, as shown by the representative spectra in Figures 3e and 3h. This is consistent with darker tones in the post-storm band depth map (indicating overall weaker green band depths).

Several studies of spectral features of the Martian surface have shown that this kind of variation in spectral reflectance is consistent with the loss of ferric dust from the scene. Johnson, Grundy, et al. (2006) compared the albedo of three surfaces before and after a dust removal event at the Spirit location; each surface presented a different spectral reflectance, but all of them showed an albedo decrease after the event. Johnson et al. (2015) analyzed the dust coating effects on the relative reflectance of surface targets, showing a decrease in the reflectance as ChemCam laser pulses removed dust from the target. Wellington et al. (2017) analyzed Mars Science Laboratory Mastcam images of two portions of the surface at Rocknest: the altered surface presented a lower albedo and a lower band depth than the undisturbed dusty surface. Rice et al. (2022) analyzed the spectral variability of dusty and dust-cleared targets, showing that dust consistently alters the spectral reflectance of the surface, approaching the spectrum of optically thick dust (higher reflectance particularly at longer wavelengths), and that dust cleared surfaces show weaker green band depths. Based on these studies of variations in the spectral reflectance of Martian surfaces, we conclude that this overall weakening of the band depth suggests that the albedo change is mainly caused by dust removal, with lesser contributions from the redistribution of larger particles.

Figures 3f and 3g show Mastcam-Z images of the region containing a rock in the TIRS FOV before and after the dust storm. Changes in the spatial distribution of dark sand on the rock surfaces were apparent after the storm, but there was also an overall darkening of the scene, which is corroborated in Figure 3h by comparison of the relative reflectance spectra (extracted from the green box in Figure 3f). Laboratory experiments using Mars-analog materials have shown that the relative reflectance increases with increasing amount of deposited dust, and that the variation is stronger at longer visible wavelengths (Johnson & Grundy, 2001; Wells et al., 1984). Hence, the observed wavelength-dependent decrease in reflectance is consistent with dust removal from the scene.

The conclusion that dust removal was the main cause of the albedo change does not imply that all of the dust from the scenes was removed or the absence of redistribution of materials from other aeolian processes. The redistribution of larger particles occurs mainly on artificially altered surfaces (wheel tracks); this is consistent with previous observations from Spirit observations (Sullivan et al., 2008), which show that the most notorious effect of dust storm activity was the erasure of wheel tracks. Hence, on some areas it is possible to identify both dust removal and sand redistribution: changes in wheel track morphology (Figures 2 and 3) were a consequence of larger grain redistributions, whereas dust removal caused an overall darkening of the tracks.

During the first half of the dust storm, strong fluctuations in the downward and upward shortwave radiation suggest significant temporal variability in atmospheric opacity and extraordinarily high mobilization of small particles (Lemmon et al., 2022). Contrary to the case of the dust devil shown in Figure 1, the drop in albedo between sols 315 and 316 is not found in the MEDA sampling; therefore, it is not possible to confirm whether the albedo change was induced by dust devils or wind gusts. The Supercam microphone acquired measurements during short periods of the dust storm. There were 9 recordings on sol 317 between 16:51 and 18:03 LTST; when compared to all microphone recordings between 15:00 and 19:00 LTST, three of them are amongst the most energetic recordings seen throughout the mission (Figure 4). These recordings occur at the upper tail of the distribution, which has a low probability of occurrence when conditioned on the overall distribution, supporting the strong winds during the dust storm.

Dust and sand redistribution at Jezero crater can be caused by both dust devils and strong wind gusts. The largest changes in albedo are associated with the dust storm. Although albedo changes caused by dust devils under typical conditions are more frequent, they also appear to be smaller both in extent and magnitude.

5. Overall Discussion

5.1. Dust Lifting Thresholds and Dependence of Albedo Change Occurrence on Dust Devil Intensity

In Section 3, we showed that not all the convective vortices capable of lifting dust generate a surface albedo change. Although the decreases in the shortwave radiation shown in Table 1 are an indicator of enhanced suspended dust,

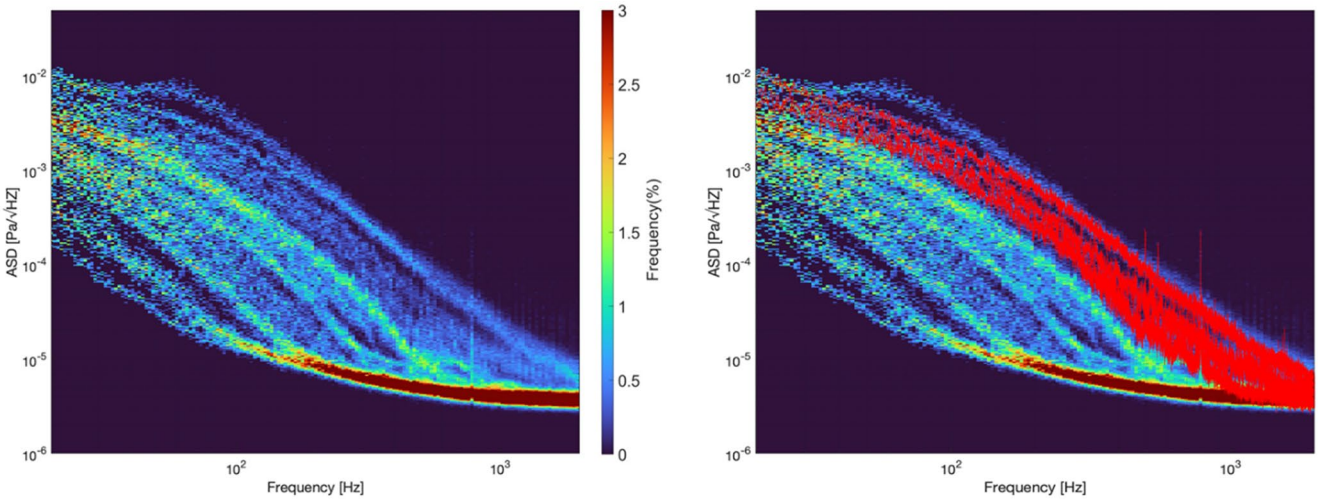

Figure 4. (left) Probabilistic distribution of the Amplitude Spectral Densities (ASD) of the Supercam microphone recordings as a function of frequency from landing to sol 317 in the period 15:00–19:00 LTST. The color code indicates the likelihood of a given spectral density, with blue being the least common. (right) As in the left panel, but with the three most energetic Supercam microphone recordings on sol 317 highlighted in red.

the conditions at the location where the dust transported by the convective vortex when it reached the rover was lofted cannot be measured. Here we focus on surface albedo changes at the TIRS FOV because MEDA measurements provide environmental variables coincident in time and space with the dust removal process, allowing a discussion on dust lifting thresholds and likelihood of surface changes as a function of vortex intensity that does not require further assumptions.

In this subsection, we further explore the features of the dust devils identified in Table 1 and their effect on surface albedo. Circles in Figure 5 represent the dust devils as a function of pressure drop, peak wind speed, decrease in shortwave radiation (circle size) and the effect on surface albedo (red circles indicate an unambiguous decrease in the reflectance). Surface albedo changes are typically caused by the most intense dust devils, characterized by pressure drops above 2.5 Pa; their potential to lift dust is corroborated by the decreases in the shortwave radiation, which are typically around or above 10%.

The probability of observing an albedo change increases with the magnitude of the pressure drop: an unambiguous albedo change was detected in 3.5% of the dust devils with a pressure drop below 2.5 Pa, in 43% of those with ΔP above 2.5 Pa, and in 100% of those with ΔP above 4.5 Pa. In order to further study the potential of generating an albedo change as a function of the dust devil intensity, we classified the dust devils listed in Table 1 as a function of pressure drop and calculated the fraction of dust devils causing albedo changes for each bin. This analysis shows an increase in the probability of detecting an albedo change with the magnitude of the pressure drop, and that this increase is more apparent for intense dust devils. These results can be compared with laboratory experiments under Martian conditions: Neakrase and Greeley (2010) showed that the dust devil sediment flux (mass of the lifted particles per unit of area and time) is closely related to ΔP. They obtained that the sediment flux is proportional to $\Delta P^{3.4}$; our conclusion of the strong effect of the dust devil intensity on the probability of generating an albedo change is consistent with their results.

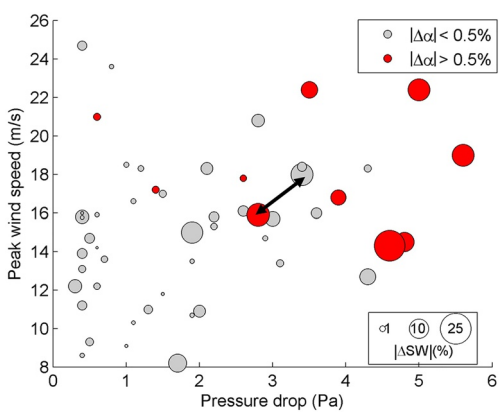

Figure 5. Scatter plot of the dust devil features presented in Section 3. Each dust devil is represented by a circle, distributed as a function of the pressure drop and peak wind speed. The size of the circle represents the measured decrease in shortwave radiation. Dust devils causing an unambiguous albedo change are highlighted in red. The black arrow connects two similar dust devils that occurred 100 min apart, which are discussed in Section 5.2.

Figure 5 also shows that none of the dust devils with peak wind speeds below 15 m/s caused an unambiguous albedo change. Above this threshold, the likelihood of changes in albedo keeps increasing with pressure drop, but differences between intense and weaker dust devils are smaller than when considering the entire data set (approximately only half of the dust devils with ΔP below 2.5 Pa present peak wind speeds above 15 m/s). Our results can be compared to those at the InSight lander location in western Elysium Planitia (4.5°N, 135.6°E;

Banerdt et al., 2020). A comparison of pairs of images acquired on different sols allowed the identification of surface changes during the first 400 sols of the mission (Charalambous et al., 2021), and candidate convective events were associated with the observed changes (Baker et al., 2021). Surface changes detected by InSight appear to be caused by intense events, most of them showing peak wind speeds above 15 m/s and pressure drops above 2 Pa (Baker et al., 2021).

Table 1 shows numerous dusty convective vortices with pressure drops below 0.1% of the ambient pressure. On Earth, Lorenz (2014) found that vortex detection from pressure measurements and visual dust devil counts lead to similar areal formation rates if dust lifting typically only occurs for $\Delta P > 30$ Pa, which represents around 0.03% of the ambient pressure. Hence, the relative pressure drop threshold needed for dust lifting appears to be similar to both planets. Contrary to the persistent changes in surface albedo, the decreases in solar radiation only last for several seconds (Figure 1b), occurring when the dust devil intercepts the direct solar radiation that reaches the RDS photodiodes. These local and transient increases in opacity detected by MEDA contribute to maintaining the background levels of suspended dust, but typically are not identified in the less frequent opacity observations acquired with Mastcam-Z or Skycam (Lemmon et al., 2022; Rodriguez-Manfredi et al., 2023).

5.2. Impact of Surface Dust Properties and Dust Removal Estimations

The intensity of the dust devil plays an important role in the generation of surface albedo changes. However, surface albedo is affected differently by dust devils with similar features. This apparently paradoxical situation occurred on sol 57, when two strong dust devils 100 min apart (connected by a double arrow in Figure 5) affected Perseverance, but only the first one caused a clear change in surface albedo. The different effects of the dust devil on the surface could be explained by differences either in the intensity, size and trajectory of the dust devils or in the surface material.

Both dust devils had similar pressure and shortwave radiation drops and wind speeds (Table 1), suggesting similar intensity and dust content. This suggests that differences in intensity are not responsible for the different effect on the surface.

We performed Monte Carlo simulations of dust devils with different intensities, sizes, and trajectories referred to MEDA and analyzed their fit to the pressure and wind measurements. The underlying model is described in Lorenz (2016), and the Monte-Carlo fit technique is explained in Hueso et al. (2023). Simulations (Figure 6) support the similarities in intensity (central pressure drop of 3.2 ± 0.3 and 3.9 ± 0.7 Pa for the first and second dust devils). There are some differences among the two events on sol 57: the second one was significantly larger (estimated diameters of 20 ± 8 vs. 9.1 ± 3.1 m for the second and first respectively), but its center passed further from MEDA (5.3 ± 3.2 vs. 1.3 ± 0.7 m). However, in both cases, simulations suggest that both dust devils completely surrounded the rover; hence, both had the potential to affect the surface in the TIRS FOV.

The clear change in surface albedo suggests that a significant fraction of dust particles was removed during the first dust devil, so that the second dust devil, although having the potential to lift dust particles, did not lift them at the region observed by TIRS (dust settling between both dust devils is expected to be negligible). Alternatively, the first dust devil could have reduced the width of the particle size distribution at the surface, making it more difficult to detect an albedo change.

The importance of surface dust availability and mobility is further corroborated by comparing with InSight landing site. Despite the similarity in the wind speed and pressure drop thresholds for dust lifting, dust devil detections from images and other solar radiation observations are significantly more frequent at Jezero than at Elysium Planitia (Lorenz, Lemmon, & Maki, 2021; Newman et al., 2022).

The intensity and proximity of the convective vortex as well as the availability of particles at the surface that could potentially be lifted appear to play a role in the ability to detect albedo changes from MEDA measurements. A devoted analysis of a future extended dust devil catalog might provide insights into the still elusive exact effect on albedo changes of dust devil size and distance to the observed surface.

Finally, we estimate the dust being removed during the events that caused surface albedo changes. Reiss et al. (2010) used microscopic images to analyze ripple surfaces inside and outside dust devil tracks observed on Earth. Their analysis showed that not all fine particles were removed from the surface affected by the dust devil, with particles remaining mainly within the pore volume of the underlying coarse sand. Unfortunately, the

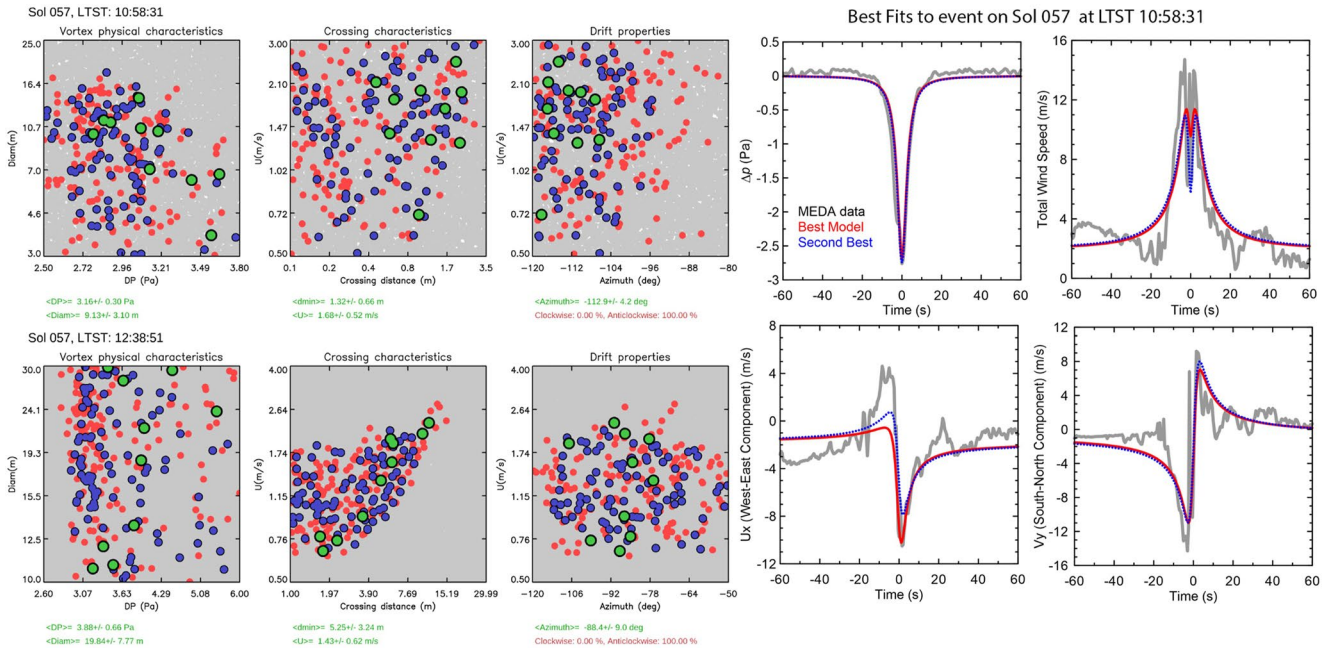

Figure 6. Monte Carlo simulations of the two dust devils on sol 57. Left six panels: Space of parameters explored. The simulations were launched in 3 rounds of 20,000 to 50,000 models covering an initially large space of parameters that includes vortex central pressures and diameters from 2.5 to 10.0 Pa and 1.0–150 m, all possible directions, wind speeds from 0.5 to 12.0 m/s, crossing distances from 0.1 to 300 m and both signs of rotation. The space of parameters shown here corresponds to results from the third and final refinement. Each exploration of the space of parameters included 15,000–50,000 models. The best 200 models that most closely fit Mars Environmental Dynamics Analyzer (MEDA) data are shown in red; the best 100 models that most closely fit MEDA pressure and wind data are shown in blue; and the 10 best models are highlighted in green; diameters and crossing distances are obtained from these 10 simulations. Right four panels: MEDA pressure and wind data compared with two of the best 10 models for the event on sol 57 at 10:58 LTST. Simulations indicate that both dust devils surrounded the rover.

resolution of Mastcam-Z images does not allow the resolution of individual dust grains. However, it is possible to perform some estimations using laboratory experiments. Using an empirical fit of surface reflectance versus dust layer thickness (Wells et al., 1984) adapted to the albedo of optically thick layers of Martian dust (Bapst et al., 2022), we obtain an equivalent dust thickness layer from

$$A_2 = 0.32 - (0.32 - A_1) \cdot e^{-2\Delta t} \quad (2)$$

Where A_1 and A_2 represent the surface albedo before and after the dust removal event, and Δt represents the change in dust thickness (in mg·cm^{-2}). For the case of the surface albedo change on sol 57, using albedo values from Table 1, we obtain a dust thickness decrease of $4.5{\cdot}10^{-3}$ mg·cm^{-2}. Assuming a canonical dust particle radius of 1.5 μm (Clancy et al., 2003; Vicente-Retortillo et al., 2017) and a density of 2,600 mg·cm^{-3} (Neakrase et al., 2006), one monolayer of dust would correspond to 0.4 mg·cm^{-2}. This would imply that approximately 1% of the surface observed by TIRS would have changed from a dust-coated to a dust-free surface.

Wells et al. (1984) also indicate that if the surface is not completely covered by dust, the reflectance depends on the relative area of the covered surface. Assuming an albedo contrast of 0.25 between bright dust covered areas and dust-free surfaces, which is consistent with observations (Ruff & Christensen, 2002), dust cover could have decreased from ∼20% to ∼19.3%, which is consistent with the previous estimation using Equation 2. The dust storm would have induced larger changes, with dust cover decreasing from 16% to 8.5%. We note that these values are estimates: the surface is not homogeneous, which allows for large amounts of dust to remain within coarse sands after dust removal events (Greeley et al., 2005; Reiss et al., 2010) and there are albedo spatial variations (albedo changes due to dust removal are difficult to observe on surfaces with similar reflectance such as optically thick dust layers). Furthermore, two-layer radiative transfer models of dust-coated surfaces reveal the strong dependence of illumination and observation angles on constraining dust thickness (Johnson, Sohl-Dickstein, et al., 2006; Johnson et al., 2003, 2004, Kinch et al., 2007, 2015; Merusi et al., 2022), which has not been considered fully here.

Nonetheless, from this analysis, it is possible to conclude that apparently very small changes in the amount of dust deposited on the surface can lead to observable changes in albedo. This is consistent with results on Earth,

where albedo decreases of 0.5%–0.6% were caused by the removal of dust with an equivalent thickness below 2 μm (Reiss et al., 2010, 2016).

5.3. Temperature Drops Associated to the Dust Removal Events: Causes and Implications

Table 1 shows that there is a surface temperature drop associated with the dust devils that caused an albedo change. Here, we discuss the potential causes and implications of these temperature drops. In order to quantify the response of the surface to changes in incoming solar radiation, we analyzed the effects of Phobos eclipse with simultaneous MEDA measurements. The eclipses on sols 397 and 398 had similar durations and caused decreases in the solar radiation reflected by the surface observed by TIRS of 8.6 and 5.6 W/m^2, which caused transient surface temperature drops of approximately 0.5 and 0.35 K: temperature shows a response that appears to be proportional to the energy deficit.

In the case of the dust devils, the relationship between the decreases in solar radiation and surface temperature is not straightforward. The weak correlation could be partly explained by the different thermophysical properties of the terrain across the rover traverse (Martínez et al., 2023). The solar energy deficit and the temperature decrease of the second dust devil on sol 57 were similar to the values during the Phobos eclipses, suggesting that in this case the temperature change could be explained mostly by the radiative imbalance. In contrast, the energy deficit of the first dust devil on sol 57 was smaller, but the decrease in ground temperature was significantly larger. This additional decrease in surface temperature could be caused by lifting and transport of surficial small particles, which would expose the cooler surface material beneath them; this effect would not occur during the second dust devil due to dust removal during the first one. Other dust devils with a similar decrease in incoming solar radiation and with clear surface albedo changes, such as those on sols 82 and 166, show similar or larger surface temperature changes than the first one on sol 57 (Table 1), supporting this hypothesis. The surface temperature drop could also be magnified by the presence of lofted particles between TIRS and the surface, which are cooled by the atmosphere. Transient surface temperature drops that are larger than the effect expected from a decrease in solar radiation could indicate lifting or transport of small particles. This would be particularly useful in regions where the photometric effect of sand transport or dust removal from the surface is small (such as surfaces with relatively thick and homogeneous layers of sand or dust).

5.4. Implications for Solar Powered Missions

Dust devils are important for long-term solar powered missions on Mars because of the removal of dust accumulated on solar panels. Predictions of dust removal events have typically been performed from satellite observations of dust devil track formation (in tracks·km^{-2}·sol^{-1}), which are then converted to the recurrence time of a dust removal event at a fixed location. In principle, a dust devil or wind gust causing a surface albedo change could remove dust from a solar panel, as was observed multiple times during the Mars Exploration Rover missions (e.g., Kinch et al., 2007, 2015). We detected 12 dust devils that could have removed dust from solar panels during the first 350 sols of the mission, all of them separated by less than 70 sols. Considering that MEDA has monitored surface albedo during approximately 52% of the time between 10 and 16 LTST (when the surface albedo changes have been detected), this would imply one event every 15 sols. Dust removal events appear to be hundreds of times more frequent than at the InSight landing site, where the recurrence time has been estimated to be above 7,000 sols (Reiss & Lorenz, 2016). This difference indicates that dust accumulation on solar panels can be strongly affected by the landing site, in agreement with previous studies from satellite and in situ measurements (Lorenz, Martínez, et al., 2021). Perseverance does not carry solar panels, but RDS measurements can provide information on the temporal evolution of dust accumulation on the photodiodes, similar to REMS UV measurements at Gale crater (Vicente-Retortillo et al., 2018, 2020). The analysis of dust accumulation on the RDS will be the subject of a future study.

6. Conclusions

We have analyzed temporal variations in surface albedo using unprecedented measurements of reflected and downwelling shortwave radiation during the first 350 sols of the Mars 2020 mission. MEDA measurements allow for unambiguous attribution of the dust lifting mechanisms inducing the albedo changes. These albedo changes are induced by dusty convective vortices and by a dust storm that affected the rover. All of the detected changes

outside the dust storm are attributed to dust devils, suggesting that this mechanism is more frequent than gust lifting in this period. The dust storm caused a 17% decrease in surface albedo, which is one order of magnitude larger than any of the more frequent unambiguous changes induced by dust devils outside dust storm conditions.

Albedo changes are typically induced by the most intense and dusty convective vortices. However, there are dust devils with similar features that do not affect the surface albedo. Our results suggest that the generation of a surface albedo change is affected by dust devil intensity (pressure drop and wind speed) and proximity, as well as dust availability and mobility at the surface. Dust devils inducing albedo changes typically show a transient drop in surface temperature; this drop, which cannot be explained solely by the decrease in shortwave radiation caused by the dust devil, could be indicative of lifting and transport of small particles. Hence, high frequency surface temperature measurements allow for the detection of local aeolian processes when terrain features mask their effect on albedo.

Mastcam-Z images support changes in the surface inferred by TIRS data during the dust storm. The magnitude of the decrease in surface reflectance increases with wavelength and the green Bayer filter band depth (related to an absorption band typically present in dusty surfaces) becomes weaker, suggesting that the albedo change can be mainly attributed to the loss of dust from the scene.

Our results show the potential of the combination of high-cadence albedo measurements covering several hours per sol with a comprehensive set of simultaneous environmental measurements and a quantitative analysis of images of the terrain and microphone recordings to improve our understanding of aeolian processes on Mars.

Data Availability Statement

MEDA measurements (Rodriguez-Manfredi & de la Torre Juarez, 2021) are stored in the NASA Planetary Data System (PDS) Atmospheres node. Mastcam-Z calibrated images (Bell & Maki, 2021) and Navcam images (Maki, 2020) are available via the NASA PDS Imaging node. Microphone data (Wiens & Maurice, 2021) are available on the NASA PDS Geosciences node. Files needed for the analysis of microphone data presented in Figure 4 and results of the Monte Carlo simulations of the dust devils on sol 57 are publicly available in Vicente-Retortillo (2023). The program used for the Monte Carlo simulations is publicly available in Hueso (2022).

Acknowledgments
This research has been funded by the Comunidad de Madrid Project S2018/NMT-4291 (TEC2SPACE-CM), by the Spanish State Research Agency (AEI) Project MDM-2017-0737 Unidad de Excelencia "María de Maeztu"- Centro de Astrobiología (CSIC/INTA), by the Spanish Ministry of Science and Innovation (MCIN)/State Agency of Research (10.13039/501100011033) project RTI2018-098728-B-C31, and by the project PID2021-126719OB-C41, funded by MCIN/AEI/10.13039/501100011033/FEDER, UE. RH, ASL and AM were supported by Grant PID2019-109467GB-I00 funded by MCIN/AEI/10.13039/501100011033/. Part of the research was carried out at the Jet Propulsion Laboratory, California Institute of Technology, under a contract with the National Aeronautics and Space Administration (80NM0018D0004). We want to thank J. Bell for processing Mastcam-Z projections showing the entire TIRS FOV and to S. Navarro and the entire team for generating the processed wind sensor data.

References

Apestigue, V., Gonzalo, A., Jiménez, J. J., Boland, J., Lemmon, M., de Mingo, J. R., et al. (2022). Radiation and dust sensor for Mars environmental dynamic analyzer onboard M2020 rover. *Sensors*, *22*(8), 2907. https://doi.org/10.3390/s22082907

Baker, M., Newman, C., Charalambous, C., Golombek, M., Spiga, A., Banfield, D., et al. (2021). Vortex-dominated Aeolian activity at InSight's landing site, Part 2: Local meteorology, transport dynamics, and model analysis. *Journal of Geophysical Research: Planets*, *126*(4), e2020JE006514. https://doi.org/10.1029/2020je006514

Banerdt, W. B., Smrekar, S. E., Banfield, D., Giardini, D., Golombek, M., Johnson, C. L., et al. (2020). Initial results from the InSight mission on Mars. *Nature Geoscience*, *13*(3), 183–189. https://doi.org/10.1038/s41561-020-0544-y

Bapst, J., Piqueux, S., Edwards, C. S., Wolfe, C., Hayne, P. O., Kass, D. M., & Kleinböhl, A. (2022). Surface dust redistribution on Mars from interannual differences in temperature and albedo. *Journal of Geophysical Research: Planets*, *127*(12), e2022JE007365. https://doi.org/10.1029/2022je007365

Basu, S., Richardson, M. I., & Wilson, R. J. (2004). Simulation of the Martian dust cycle with the GFDL Mars GCM. *Journal of Geophysical Research*, *109*(E11), E11006. https://doi.org/10.1029/2004je002243

Bell, J. F., III., Rice, M. S., Johnson, J. R., & Hare, T. M. (2008). Surface albedo observations at Gusev crater and Meridiani Planum, Mars. *Journal of Geophysical Research*, *113*(E6), E06S18. https://doi.org/10.1029/2007je002976

Bell, J. F., & Maki, J. N. (2021). Calibrated data products for the Mars 2020 Perseverance rover mast camera zoom camera created by the Arizona State University Mastcam-Z instrument team for the science team. *NASA Planetary Data System Imaging Node*. https://doi.org/10.17189/q3ts-c749

Bell, J. F., Maki, J. N., Mehall, G. L., Ravine, M. A., Caplinger, M. A., Bailey, Z. J., et al. (2021). The Mars 2020 perseverance rover mast camera zoom (Mastcam-Z) multispectral, stereoscopic imaging investigation. *Space Science Reviews*, *217*(1), 1–40. https://doi.org/10.1007/s11214-020-00755-x

Cantor, B. A., Kanak, K. M., & Edgett, K. S. (2006). Mars Orbiter Camera observations of Martian dust devils and their tracks (September 1997 to January 2006) and evaluation of theoretical vortex models. *Journal of Geophysical Research*, *111*(E12), E12002. https://doi.org/10.1029/2006je002700

Charalambous, C., McClean, J. B., Baker, M., Pike, W. T., Golombek, M., Lemmon, M., et al. (2021). Vortex-dominated Aeolian activity at InSight's Landing Site, Part 1: Multi-instrument observations, analysis, and implications. *Journal of Geophysical Research: Planets*, *126*(6), e2020JE006757. https://doi.org/10.1029/2020je006757

Chide, B., Murdoch, N., Bury, Y., Maurice, S., Jacob, X., Merrison, J. P., et al. (2021). Experimental wind characterization with the SuperCam microphone under a simulated Martian atmosphere. *Icarus*, *354*, 114060. https://doi.org/10.1016/j.icarus.2020.114060

Clancy, R. T., Wolff, M. J., & Christensen, P. R. (2003). Mars aerosol studies with the MGS TES emission phase function observations: Optical depths, particle sizes, and ice cloud types versus latitude and solar longitude. *Journal of Geophysical Research*, *108*(E9), 5098. https://doi.org/10.1029/2003je002058

Farley, K. A., Williford, K. H., Stack, K. M., Bhartia, R., Chen, A., de la Torre, M., et al. (2020). Mars 2020 mission overview. *Space Science Reviews*, *216*(8), 1–41. https://doi.org/10.1007/s11214-020-00762-y

Farrand, W. H., Bell, J. F., III., Johnson, J. R., Squyres, S. W., Soderblom, J., & Ming, D. W. (2006). Spectral variability among rocks in visible and near-infrared multispectral Pancam data collected at Gusev crater: Examinations using spectral mixture analysis and related techniques. *Journal of Geophysical Research*, *111*(E2), E02S15. https://doi.org/10.1029/2005JE002495

Fenton, L., Reiss, D., Lemmon, M., Marticorena, B., Lewis, S., & Cantor, B. (2016). Orbital observations of dust lofted by daytime convective turbulence. *Space Science Reviews*, *203*(1), 89–142. https://doi.org/10.1007/s11214-016-0243-6

Geissler, P. E., Fenton, L. K., Enga, M. T., & Mukherjee, P. (2016). Orbital monitoring of Martian surface changes. *Icarus*, *278*, 279–300. https://doi.org/10.1016/j.icarus.2016.05.023

Greeley, R., Arvidson, R., Bell, J. F., III., Christensen, P., Foley, D., Haldemann, A., et al. (2005). Martian variable features: New insight from the Mars express orbiter and the Mars exploration rover spirit. *Journal of Geophysical Research*, *110*(E6), E06002. https://doi.org/10.1029/2005je002403

Harri, A. M., Genzer, M., Kemppinen, O., Kahanpää, H., Gomez-Elvira, J., Rodriguez-Manfredi, J. A., et al. (2014). Pressure observations by the Curiosity rover: Initial results. *Journal of Geophysical Research: Planets*, *119*(1), 82–92. https://doi.org/10.1002/2013je004423

Hayes, A. G., Corlies, P., Tate, C., Barrington, M., Bell, J. F., Maki, J. N., et al. (2021). Pre-flight calibration of the Mars 2020 rover Mastcam zoom (Mastcam-Z) multispectral, stereoscopic imager. *Space Science Reviews*, *217*(2), 1–95. https://doi.org/10.1007/s11214-021-00795-x

Hueso (2022). General tools for analysis of convective vortices (IDL and Fortran codes) (0.9). *Zenodo*. https://doi.org/10.5281/zenodo.6958141

Hueso, R., Newman, C. E., del Río-Gaztelurrutia, T., Munguira, A., Sánchez-Lavega, A., Toledo, D., et al. (2023). Convective vortices and dust devils detected and characterized by Mars 2020. *Journal of Geophysical Research: Planets*, *128*(2), e2022JE007516. https://doi.org/10.1029/2022je007516

Jacob, S. R., Wellington, D. F., Bell, J. F., Achilles, C., Fraeman, A. A., Horgan, B., et al. (2020). Spectral, compositional, and physical properties of the Upper Murray formation and Vera Rubin ridge, Gale crater, Mars. *Journal of Geophysical Research: Planets*, *125*(11), e2019JE006290. https://doi.org/10.1029/2019je006290

Johnson, J. R., Bell, J. F., Bender, S., Blaney, D., Cloutis, E., DeFlores, L., et al. (2015). ChemCam passive reflectance spectroscopy of surface materials at the Curiosity landing site, Mars. *Icarus*, *249*, 74–92. https://doi.org/10.1016/j.icarus.2014.02.028

Johnson, J. R., & Grundy, W. M. (2001). Visible/near-infrared spectra and two-layer modeling of palagonite-coated basalts. *Geophysical Research Letters*, *28*(10), 2101–2104. https://doi.org/10.1029/2000gl012669

Johnson, J. R., Grundy, W. M., & Lemmon, M. T. (2003). Dust deposition at the Mars Pathfinder landing site: Observations and modeling of visible/near-infrared spectra. *Icarus*, *163*(2), 330–346. https://doi.org/10.1016/s0019-1035(03)00084-8

Johnson, J. R., Grundy, W. M., Lemmon, M. T., Bell, J. F., III, Johnson, M. J., Deen, R. G., et al. (2006). Spectrophotometric properties of materials observed by Pancam on the Mars exploration rovers: 1. Spirit. *Journal of Geophysical Research*, *111*(E2), 114261. https://doi.org/10.1029/2005je002494

Johnson, J. R., Grundy, W. M., & Shepard, M. K. (2004). Visible/near-infrared spectrogoniometric observations and modeling of dust-coated rocks. *Icarus*, *171*(2), 546–556. https://doi.org/10.1016/j.icarus.2004.05.013

Johnson, J. R., Sohl-Dickstein, J., Grundy, W. M., Arvidson, R. E., Bell, J. F., III., Christensen, P., et al. (2006). Radiative transfer modeling of dust-coated Pancam calibration target materials: Laboratory visible/near-infrared spectrogoniometry. *Journal of Geophysical Research*, *111*(E12), E12S07. https://doi.org/10.1029/2005je002658

Kahre, M. A., Murphy, J. R., & Haberle, R. M. (2006). Modeling the Martian dust cycle and surface dust reservoirs with the NASA Ames general circulation model. *Journal of Geophysical Research*, *111*(E6), E06008. https://doi.org/10.1029/2005je002588

Kahre, M. A., Murphy, J. R., Newman, C. E., Wilson, R. J., Cantor, B. A., Lemmon, M. T., & Wolff, M. J. (2017). The Mars dust cycle. In R. Haberle, R. T. Clancy, F. Forget, M. D. Smith, & R. W. Zurek (Eds.), *The atmosphere and climate of Mars* (pp. 295–337). Cambridge Univ. Press.

Kinch, K. M., Bell, J. F., III., Goetz, W., Johnson, J. R., Joseph, J., Madsen, M. B., & Sohl-Dickstein, J. (2015). Dust deposition on the decks of the Mars exploration rovers: 10 years of dust dynamics on the panoramic camera calibration targets. *Earth and Space Science*, *2*(5), 144–172. https://doi.org/10.1002/2014ea000073

Kinch, K. M., Sohl-Dickstein, J., Bell, J. F., III., Johnson, J. R., Goetz, W., & Landis, G. A. (2007). Dust deposition on the Mars exploration rover panoramic camera (Pancam) calibration targets. *Journal of Geophysical Research*, *112*(E6), E06S03. https://doi.org/10.1029/2006je002807

Lemmon, M. T., Smith, M. D., Viudez-Moreiras, D., de la Torre-Juarez, M., Vicente-Retortillo, A., Munguira, A., et al. (2022). Dust, sand, and winds within an active Martian storm in Jezero crater. *Geophysical Research Letters*, *49*(17), e2022GL100126. https://doi.org/10.1029/2022gl100126

Lorenz, R. D. (2014). Vortex encounter rates with fixed barometer stations: Comparison with visual dust devil counts and large-eddy simulations. *Journal of the Atmospheric Sciences*, *71*(12), 4461–4472. https://doi.org/10.1175/jas-d-14-0138.1

Lorenz, R. D. (2016). Heuristic estimation of dust devil vortex parameters and trajectories from single-station meteorological observations: Application to InSight at Mars. *Icarus*, *271*, 326–337. https://doi.org/10.1016/j.icarus.2016.02.001

Lorenz, R. D., Lemmon, M. T., & Maki, J. (2021). First Mars year of observations with the InSight solar arrays: Winds, dust devil shadows, and dust accumulation. *Icarus*, *364*, 114468. https://doi.org/10.1016/j.icarus.2021.114468

Lorenz, R. D., Martínez, G. M., Spiga, A., Vicente-Retortillo, A., Newman, C. E., Murdoch, N., et al. (2021). Lander and rover histories of dust accumulation on and removal from solar arrays on Mars. *Planetary and Space Science*, *207*, 105337. https://doi.org/10.1016/j.pss.2021.105337

Maki, J. N. (2020). Calibrated data products for the Mars 2020 perseverance rover navigation cameras. *NASA Planetary Data System Imaging Node*. https://doi.org/10.17189/yvkm-rx37

Maki, J. N., Gruel, D., McKinney, C., Ravine, M. A., Morales, M., Lee, D., et al. (2020). The Mars 2020 engineering cameras and microphone on the perseverance rover: A next-generation imaging system for Mars exploration. *Space Science Reviews*, *216*(8), 1–48. https://doi.org/10.1007/s11214-020-00765-9

Malin, M. C., & Cantor, B. A. (2022). MRO MARCI weather report for the week of 3 January 2022–9 January 2022, Malin space science systems captioned image release, MSSS 432 604. Retrieved from http://www.msss.com/msss_images/2022/01/12/

Martínez, G. M., Sebastián, E., Vicente-Retortillo, A., Smith, M. D., Johnson, J. R., Fischer, E., et al. (2023). Surface energy budget, albedo and thermal inertia at Jezero Crater, Mars, as observed from the Mars 2020 MEDA instrument. *Journal of Geophysical Research: Planets*, *128*(2), e2022JE007537. https://doi.org/10.1029/2022je007537

Maurice, S., Wiens, R. C., Bernardi, P., Caïs, P., Robinson, S., Nelson, T., et al. (2021). The SuperCam instrument suite on the Mars 2020 rover: Science objectives and Mast-Unit description. *Space Science Reviews*, *217*(3), 1–108.

Merusi, M., Kinch, K. B., Madsen, M. B., Bell, J. F., Maki, J. N., Hayes, A. G., et al. (2022). The Mastcam-Z radiometric calibration targets on NASA's Perseverance rover: Derived irradiance time-series, dust deposition, and performance over the first 350 sols on Mars. *Earth and Space Science*, *9*(12), e2022EA002552. https://doi.org/10.1029/2022ea002552

Morris, R. V., Golden, D. C., Bell, J. F., III., Shelfer, T. D., Scheinost, A. C., Hinman, N. W., et al. (2000). Mineralogy, composition, and alteration of Mars Pathfinder rocks and soils: Evidence from multispectral, elemental, and magnetic data on terrestrial analogue, SNC meteorite, and Pathfinder samples. *Journal of Geophysical Research*, *105*(E1), 1757–1817. https://doi.org/10.1029/1999je001059

Neakrase, L. D., & Greeley, R. (2010). Dust devil sediment flux on Earth and Mars: Laboratory simulations. *Icarus*, *206*(1), 306–318. https://doi.org/10.1016/j.icarus.2009.08.028

Neakrase, L. D. V., Greeley, R., Iversen, J. D., Balme, M. R., & Eddlemon, E. E. (2006). Dust flux within dust devils: Preliminary laboratory simulations. *Geophysical Research Letters*, *33*(19), L19S09. https://doi.org/10.1029/2006gl026810

Newman, C. E., Hueso, R., Lemmon, M. T., Munguira, A., Vicente-Retortillo, Á., Apestigue, V., et al. (2022). The dynamic atmospheric and Aeolian environment of Jezero crater, Mars. *Science Advances*, *8*(21), eabn3783.

Newman, C. E., Lewis, S. R., Read, P. L., & Forget, F. (2002a). Modeling the Martian dust cycle, 1. Multiannual radiatively active dust transport simulations. *Journal of Geophysical Research*, *107*(E12), 6–1. https://doi.org/10.1029/2002je001910

Newman, C. E., Lewis, S. R., Read, P. L., & Forget, F. (2002b). Modeling the Martian dust cycle 2. Multiannual radiatively active dust transport simulations. *Journal of Geophysical Research*, *107*(E12), 7–1. https://doi.org/10.1029/2002je001920

Pérez-Izquierdo, J., Sebastián, E., Martínez, G. M., Bravo, A., Ramos, M., & Manfredi, J. A. R. (2018). The Thermal Infrared Sensor (TIRS) of the Mars Environmental Dynamics Analyzer (MEDA) instrument onboard Mars 2020, a general description and performance analysis. *Measurement*, *122*, 432–442. https://doi.org/10.1016/j.measurement.2017.12.004

Reid, R. J., Smith, P. H., Lemmon, M., Tanner, R., Burkland, M., Wegryn, E., et al. (1999). Imager for Mars Pathfinder (IMP) image calibration. *Journal of Geophysical Research*, *104*(E4), 8907–8925. https://doi.org/10.1029/1998je900011

Reiss, D., Fenton, L., Neakrase, L., Zimmerman, M., Statella, T., Whelley, P., et al. (2016). Dust devil tracks. *Space Science Reviews*, *203*(1), 143–181. https://doi.org/10.1007/s11214-016-0308-6

Reiss, D., & Lorenz, R. D. (2016). Dust devil track survey at Elysium Planitia, Mars: Implications for the InSight landing sites. *Icarus*, *266*, 315–330. https://doi.org/10.1016/j.icarus.2015.11.012

Reiss, D., Raack, J., Rossi, A. P., Di Achille, G., & Hiesinger, H. (2010). First in-situ analysis of dust devil tracks on Earth and their comparison with tracks on Mars. *Geophysical Research Letters*, *37*(14). https://doi.org/10.1029/2010gl044016

Rice, M. S., Reynolds, M., Studer-Ellis, G., Bell, J. F., III., Johnson, J. R., Herkenhoff, K. E., et al. (2018). The albedo of Mars: Six Mars years of observations from Pancam on the Mars exploration rovers and comparisons to MOC, CTX and HiRISE. *Icarus*, *314*, 159–174. https://doi.org/10.1016/j.icarus.2018.05.017

Rice, M. S., Seeger, C., Bell, J., Calef, F., St. Clair, M., Eng, A., et al. (2022). Spectral diversity of rocks and soils in Mastcam observations along the Curiosity rover's traverse in Gale crater, Mars. *Journal of Geophysical Research: Planets*, *127*(8), e2021JE007134. https://doi.org/10.1029/2021je007134

Rodriguez-Manfredi, J. A., & de la Torre Juarez, M. (2021). Mars 2020 perseverance rover Mars environmental dynamics analyzer (MEDA) experiment data record (EDR) and reduced data record (RDR) data products archive bundle. *NASA Planetary Data System Atmospheres Node*. https://doi.org/10.17189/1522849

Rodriguez-Manfredi, J. A., de la Torre Juarez, M., Sanchez-Lavega, A., Hueso, R., Martinez, G., Lemmon, M. T., et al. (2023). The diverse meteorology of Jezero crater over the first 250 sols of Perseverance on Mars. *Nature Geoscience*, *16*, 19–28.

Rodriguez-Manfredi, J. A., De la Torre Juárez, M., Alonso, A., Apéstigue, V., Arruego, I., Atienza, T., et al. (2021). The Mars Environmental Dynamics Analyzer, MEDA. A suite of environmental sensors for the Mars 2020 mission. *Space Science Reviews*, *217*(3), 1–86.

Ruff, S. W., & Christensen, P. R. (2002). Bright and dark regions on Mars: Particle size and mineralogical characteristics based on Thermal emission spectrometer data. *Journal of Geophysical Research*, *107*(E12), 5119–5122. https://doi.org/10.1029/2001je001580

Sebastián, E., Martínez, G., Ramos, M., Haenschke, F., Ferrándiz, R., Fernández, M., & Manfredi, J. A. R. (2020). Radiometric and angular calibration tests for the MEDA-TIRS radiometer onboard NASA's Mars 2020 mission. *Measurement*, *164*, 107968. https://doi.org/10.1016/j.measurement.2020.107968

Sebastián, E., Martínez, G., Ramos, M., Pérez-Grande, I., Sobrado, J., & Manfredi, J. A. R. (2021). Thermal calibration of the MEDA-TIRS radiometer onboard NASA's Perseverance rover. *Acta Astronautica*, *182*, 144–159. https://doi.org/10.1016/j.actaastro.2021.02.006

Sullivan, R., Arvidson, R., Bell, J. F., III., Gellert, R., Golombek, M., Greeley, R., et al. (2008). Wind-driven particle mobility on Mars: Insights from Mars exploration rover observations at "El Dorado" and surroundings at Gusev Crater. *Journal of Geophysical Research*, *113*(E6), E06S07. https://doi.org/10.1029/2008je003101

Szwast, M. A., Richardson, M. I., & Vasavada, A. R. (2006). Surface dust redistribution on Mars as observed by the Mars Global Surveyor and Viking orbiters. *Journal of Geophysical Research*, *111*(E11), E11008. https://doi.org/10.1029/2005je002485

Toledo, D., Apéstigue, V., Arruego, I., Lemmon, M., Gómez, L., Montoro, A. D. F., et al. (2023). Dust devil frequency of occurrence and radiative effects at Jezero crater, Mars, as measured by MEDA Radiation and Dust Sensor (RDS). *Journal of Geophysical Research: Planets*, *128*(1), e2022JE007494. https://doi.org/10.1029/2022je007494

Vicente-Retortillo, A. (2023). Derived data supporting the analysis of surface albedo changes from Mars 2020 observations: Probabilistic distribution of the Amplitude Spectral Densities of Supercam microphone recordings and Monte-Carlo dust devil simulations. (Version 1) [Dataset]. Zenodo. https://doi.org/10.5281/zenodo.7689351

Vicente-Retortillo, Á., Martínez, G. M., Renno, N., Newman, C. E., Ordonez-Etxeberria, I., Lemmon, M. T., et al. (2018). Seasonal deposition and lifting of dust on Mars as observed by the Curiosity rover. *Scientific Reports*, *8*(1), 1–8. https://doi.org/10.1038/s41598-018-35946-8

Vicente-Retortillo, Á., Martínez, G. M., Renno, N. O., Lemmon, M. T., & de la Torre-Juárez, M. (2017). Determination of dust aerosol particle size at Gale Crater using REMS UVS and Mastcam measurements. *Geophysical Research Letters*, *44*(8), 3502–3508. https://doi.org/10.1002/2017gl072589

Vicente-Retortillo, A., Martínez, G. M., Rennó, N. O., Lemmon, M. T., de la Torre-Juárez, M., & Gómez-Elvira, J. (2020). In situ UV measurements by MSL/REMS: Dust deposition and angular response corrections. *Space Science Reviews*, *216*(5), 97. https://doi.org/10.1007/s11214-020-00722-6

Wellington, D. F., & Bell, J. F., III. (2020). Patterns of surface albedo changes from Mars reconnaissance orbiter Mars color imager (MARCI) observations. *Icarus*, *349*, 113766. https://doi.org/10.1016/j.icarus.2020.113766

Wellington, D. F., Bell, J. F., Johnson, J. R., Kinch, K. M., Rice, M. S., Godber, A., et al. (2017). Visible to near-infrared MSL/Mastcam multispectral imaging: Initial results from select high-interest science targets within Gale Crater, Mars. *American Mineralogist*, *102*(6), 1202–1217. https://doi.org/10.2138/am-2017-5760ccby

Wells, E., Veverka, J., & Thomas, P. (1984). Mars: Experimental study of albedo changes caused by dust fallout. *Icarus*, *58*(3), 331–338. https://doi.org/10.1016/0019-1035(84)90079-4

Whelley, P. L., & Greeley, R. (2008). The distribution of dust devil activity on Mars. *Journal of Geophysical Research*, *113*(E7), E07002. https://doi.org/10.1029/2007je002966

Wiens, R. C., & Maurice, S. A. (2021). Mars 2020 perseverance rover SuperCam raw, calibrated, and derived data products. *NASA PDS Geosciences Node*. https://doi.org/10.17189/1522646